ACS OMEGA

Open Access

http://pubs.acs.org/journal/acsodf

Article

Comprehensive Study of Lithium Diffusion in Si/C-Layer and Si/C_3N_4 Composites in a Faceted Crystalline Silicon Anode for Fast-Charging Lithium-Ion Batteries

Ali Lashani Zand, Amin Niksirat, Zeinab Sanaee,* and Mahdi Pourfath*

Cite This: *ACS Omega* 2023, 8, 44698−44707

Read Online

ACCESS | Metrics & More | Article Recommendations

ABSTRACT: By using silicon (Si) as an anode of lithium-ion batteries, the capacity can be significantly increased, but relatively large volume expansion limits the application as an efficient anode material. Huge volume expansion of the silicon anode during lithiation, however, leads to cracking and losing its connection with the current collector. This shortcoming can be improved by the deposition of a nanometric carbon- or nitrogen-doped carbon coating on the silicon surface, resulting in Si/C-layer and Si/C_3N_4 interfaces. In this work, Li^+ diffusion in Si/C-layer and Si/C_3N_4 composite materials along three Si surfaces and various ion pathways were carefully analyzed by using density functional theory and ab initio molecular dynamic (AIMD) simulations. Both Si/C and Si/C_3N_4 interfaces and three Si surfaces of (100), (110), and (111) were investigated. The formation of nitrogen holes and monatomic carbon binders in the composite increases ion diffusivity and limits volume expansion. Furthermore, the Bader analysis shows that the type and orientation of the surfaces have important effects on ion distribution. The results indicated that the C_3N_4 composite increases Li^+ diffusion in Si (100) from 7.82×10^{-5} to 3.17×10^{-4} cm^2/s. The presented results provide a guide for the appropriate design of stable and safe high-energy-density batteries.

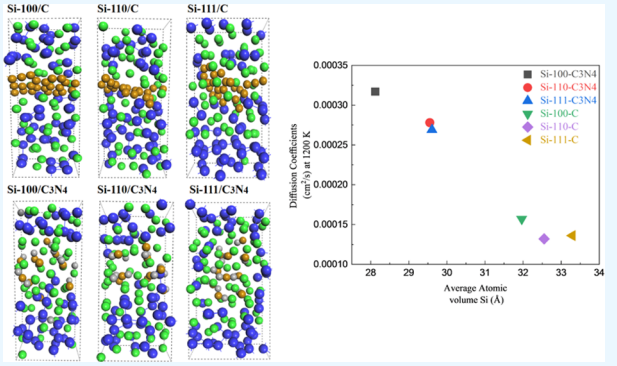

1. INTRODUCTION

Developments of portable electronic devices and electric vehicles require high-energy-density rechargeable batteries.[1,2] Rechargeable lithium-based batteries have been used for several decades in various portable electronic devices. Currently, the anode material of commercial lithium-ion batteries is mainly based on graphite with a theoretical specific capacity of (372 $mAhg^{-1}$),[2] which limits the energy density of lithium-based batteries.[3] Silicon (Si) with a high specific capacity of (3590 $mAhg^{-1}$)[4] is being considered as an alternative to graphite. Si has the potential to advance sustainable energy solutions by offering environmentally friendly and cost-effective technologies that can contribute to the low-carbon economy.[5] However, it suffers from high volume variation[6] and poor ion conductivity.[7] The massive volume change (nearly ∼300%)[8] of Si during the charging/discharging process causes mechanical fracture and destruction of the crystal,[9] which in turn lead to safety issues, capacity loss, and limited life cycles.[10] By the appropriate engineering of Li^+-ion diffusion, these problems can be suppressed. The pathway and the incident angle between the barrier and Li^+ diffusion direction can significantly affect the Li^+ diffusion characteristics in Si anodes.[11] The geometry of the host structure is effective in the distribution of guest ions in such a way that smaller incident angles result in effectively reduced scattering of Li ions in Si structures.[10]

Improving the efficiency of the Si anode requires increasing the ion diffusivity and conductivity, which can arise from a softer and more polarizable anionic framework.[12] The diffusivity of Si can be considered an important factor and when becomes as fast as Li, the stress generated during Li^+ diffusion can be partially reduced.[13] Moreover, a higher ion conductivity can accelerate the lithiation reactions and avoid uneven deposition of lithium at high current densities,[14] thereby preventing the formation of lithium dendrites.[15]

To improve the interaction of the anode materials with Li ions, nanostructuring of the anode material can be used as an effective approach.[16] The addition of carbon and nitrogen nanostructures to the silicon anode can increase the lithium-ion diffusion rate in silicon.[17] This enhancement is due to the formation of a single layer of g-C_3N_4, which shows a high ion

Received: July 28, 2023
Revised: October 24, 2023
Accepted: October 27, 2023
Published: November 14, 2023

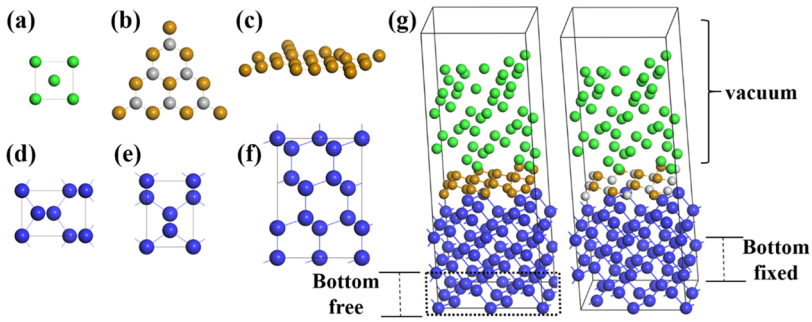

Figure 1. Initial unit cell of (a) Li, (b) amorphous carbon (a-C), (c) graphitic carbon nitride (g-C_3N_4), (d) Si (100), (e) Si (110), (f) Si (111), and composite structures of (g) Si/a-C and Si/C_3N_4. The unit cell of the composite structure with Si (100) and (110) share the same length, width, and height of 10.86 Å × 7.68 Å × 24.79 Å, while that for Si (111) are 13.30 Å × 7.68 × 27.62 Å. The unit cell of Si in the composite material consists of 56 Si atoms for (111) and 48 atoms for (100) and (110) that were relaxed from the corresponding surfaces of the 2 × 2 × 2 Si supercell. a-C-layer and g-C_3N_4 have thicknesses of 2.06 and 2.12 Å, respectively, with 24 carbon atoms for Si (100) and (110) and 26 carbon atoms for Si (111). g-C_3N_4 includes 9 nitrogen atoms and 15 carbon atoms for Si (100) and (110) and 10 nitrogen atoms and 16 carbon atoms for Si (111). Gray, blue, brown, and green spheres represent N, Si, and C atoms and Li^+, respectively. The bottom bonds of silicon atoms were passivated with hydrogen atoms.

conductivity, during the interaction of Li^+ with C and N atoms. The advanced forms of the Si anode and various carbonaceous materials, including graphite, graphene, and amorphous carbon, have been adopted as buffer matrices for Si composites to alleviate volume changes, block direct exposure of the Si surface to the electrolyte, and provide ionic conductive channels.[18] Shih et al. investigated the improvement of volume changes of Si/graphite composite by applying a spray-dried 3D spherical-like anode for the high rate and cycles Li^+-ion batteries.[19] Huo et al. showed that carbon in powder-pressed Si anodes does not only improve the ionic and electronic transport during cycling but also changes the electro-chemomechanical performance.[3] In these composites, the interfaces between Si and carbon (C) reduce interfacial charge-transfer resistance, which enhances lithiation/delithiation reactions and improves the guest-ion penetration rate.[20]

The atomistic underpinnings of this nonequilibrium electrochemical amorphization process are of interest and have been experimentally studied.[15,21−23] Cao et al. suggested that the mechanism of lithiation in the layer-by-layer method proceeds quite differently along the ⟨100⟩, ⟨110⟩, and ⟨111⟩ directions,[23] but a deep understanding of this process is missing. Due to the low *Z*-value of lithium, experimental methods to identify the diffusion behavior of Li^+ and the interaction with the atoms of the host structure were not sufficient and theoretical studies are required.[24] Ab initio molecular dynamic (AIMD) calculations are the most widely used approach for investigating various properties of materials and structures at an atomistic level.[25] AIMD calculations have been extensively applied to study lithium insertion in the anode of batteries,[25] showing that the lithiation phases for different orientations affect the amorphization process,[27,28] which leads to the formation of a structurally and compositionally different solid electrolyte interface (SEI).[29] In the present study, a comprehensive analysis of Li^+ diffusion properties of two representative phases of representative phases Si/C and ternary Si/C/N composites for three Si surfaces (100), (110), and (111) is presented by employing AIMD.

2. COMPUTATIONAL METHODS

The diffusion of Li^+ in Si/C and Si/C_3N_4 ternary composite in three surfaces of (100), (110), and (111) was investigated by utilizing the density functional theory (DFT) calculations as implemented in the Vienna ab initio simulation package (VASP).[30] The projector-augmented wave method was used to describe the interaction between core and valence electrons, and the generalized gradient approximation (GGA) based on the Perdew−Burke−Ernzerhof (PBE)[46] function was applied for the electron exchange−correlation. An energy cutoff of 300 eV was used for the expansion of the plane waves. All of the studied structures based on ab initio molecular dynamic (AIMD) simulations were optimized based on the conjugate gradient method with convergence criteria of a residual force smaller than 0.01 eV/Å and an energy change per atom smaller than 10^{-4} eV. *k*-point meshes of 3 × 2 × 1 for Si (111) and 2 × 3 × 1 for (100) and (110) surfaces in the Monkhorst−Pack scheme for sampling of the Brillouin zone were used. To analyze Li^+ diffusion and chemical lithiation processes, AIMD simulations with the canonical ensemble (NVT) were performed at a temperature of 1200 K. A time step of 1 fs and a Nosé−Hoover thermostat were used to control the temperature.

The initial unit cell of each component and the resulting composite structure are depicted in Figure 1. The initial C-layer structure was generated based on an amorphous carbon (a-C) material from Materials Project[31] and relaxed before being placed at the surface of Si atoms. The structure of g-C_3N_4 was obtained by the substitution of carbon atoms with nitrogen. The initial Si/C-layer and Si/C_3N_4 composite interfacial gap was set at 1.5 Å, which is optimized for the slab model with a 14 Å vacuum space to ensure minimal interfacial energy after the relaxation process. The vacuum space above the carbon layer was then filled with 48 amorphous Li^+ for Si (100) and Si (110) and 56 amorphous Li^+ for Si (111).

3. RESULTS AND DISCUSSION

The induced stress in the Si anode during the lithiation can be reduced if Si atoms diffuse similarly or faster than Li^+ and form reversible phases.[7] A deep understanding of the interactions between Li^+ and Si lattice and the diffusion kinetics of both species in the electrode allows us to design Si-based anodes for LiBs.[13] Although Si and graphite electrodes reduce the potential of electrolytes by the same value, they show different

https://doi.org/10.1021/acsomega.3c05523
ACS Omega 2023, 8, 44698−44707

passivation behaviors,[32] and combining two materials during lithiation creates new opportunities.

3.1. Li^+ Diffusion Behavior in c-Si, a-C, and g-C_3N_4. Li^+ diffusion in three pure crystalline Si surfaces and a-C and g-C_3N_4 were analyzed. The Li^+-ion diffusion (lithiation process) was modeled by AIMD for 5 ps with 1 fs time steps at a temperature of 1200 K. The dynamics of the amorphization during the lithiation process were analyzed by the radial distribution function (RDF). Various stages of amorphization for different crystalline silicon surfaces as well as the evolution of Li−Si and Li−Li pair correlations are shown in Figure 2a−c. The increase in the number of Li/Si pairs during the lithiation process indicates that both Si−Si bonds and Li/Li pairs were broken and Si−Li bonds were formed. After the lithiation process, the amorphization phenomenon, which leads to the formation of different a-LiSi phases, was observed in all three studied surfaces (Figure 2c). Chan et al.[26] have also shown that the RDF graphs of Si/Li and Li/Li pairs for different surfaces of crystalline Si were very similar to amorphous Si after ∼5 ps.

The RDF analysis reveals that the numbers of both Si/Si and Li/Li pairs decrease during the lithiation; however, this behavior is not the same for different Si surfaces. The nearest neighbors' Si/Si pairs were observed at interparticle distances of 2.27, 2.32, and 2.29 Å for the (100), (110), and (111) Si surfaces, respectively, see Figure 2a−c. The smooth RDF peak of the (110) surface compared with those of other surfaces is an indication that the effect of lithiation is more pronounced for this Si surface.

Figure 2d indicates that the layered structure of a-C bulk is only weakly affected after lithiation, whereas the initial structure of the g-C_3N_4 composite was completely distorted during the lithiation process. This behavior can be explained by the fact that Li^+ diffusion in carbon material usually requires an ion channel that is formed by the carbon matrix, similar to multilayer graphene and graphite.[4]

In the a-C structure, the bonds between carbon and carbon are stronger than carbon and nitrogen bonds in the g-C_3N_4 composite. After lithiation, the C/N pairs were observed at a closer distance than that of the initial structure (Figure 2e), which indicates the contraction of the structure. During lithiation, the a-C-layer disperses at a speed much lower than that of g-C_3N_4, which effectively creates a buffer layer at the beginning of the process. However, in g-C_3N_4, the bonds between carbon and nitrogen atoms were broken at the beginning of lithiation and the Li−C_3N_4 phase was formed, see Figure 2d,e. The structural changes of the a-C-layer during lithiation are much smaller than that of g-C_3N_4, which results in a longer lifespan.

3.2. Li^+ Diffusion Behavior in Composites. Amorphization of the Si/C-layer and Si/C_3N_4 composite was analyzed during the lithiation process for the three Si surfaces. Figure 3 shows that Li^+ gradually diffused into the Si material by breaking and expanding the Si−Si bonds. The C-layer also suffered from severe fluctuations during the lithiation process, such that some of the C−C bonds were broken. Li, C, and Si atoms were completely mixed after 15 ps, which indicates that 25 ps of AIMD simulation is sufficient for completing the lithiation process. Figure 3 shows that Li^+ ions diffuse into the Si lattice. Although the Si surfaces were covered by the C-layer, Li^+ could pass through the C-layer via the ion channels formed during the relaxation process. These ion channels in Si/C (110) are parallel to the Li^+ diffusion direction, whereas in Si/C (111) they are perpendicular to the Li^+ diffusion direction.

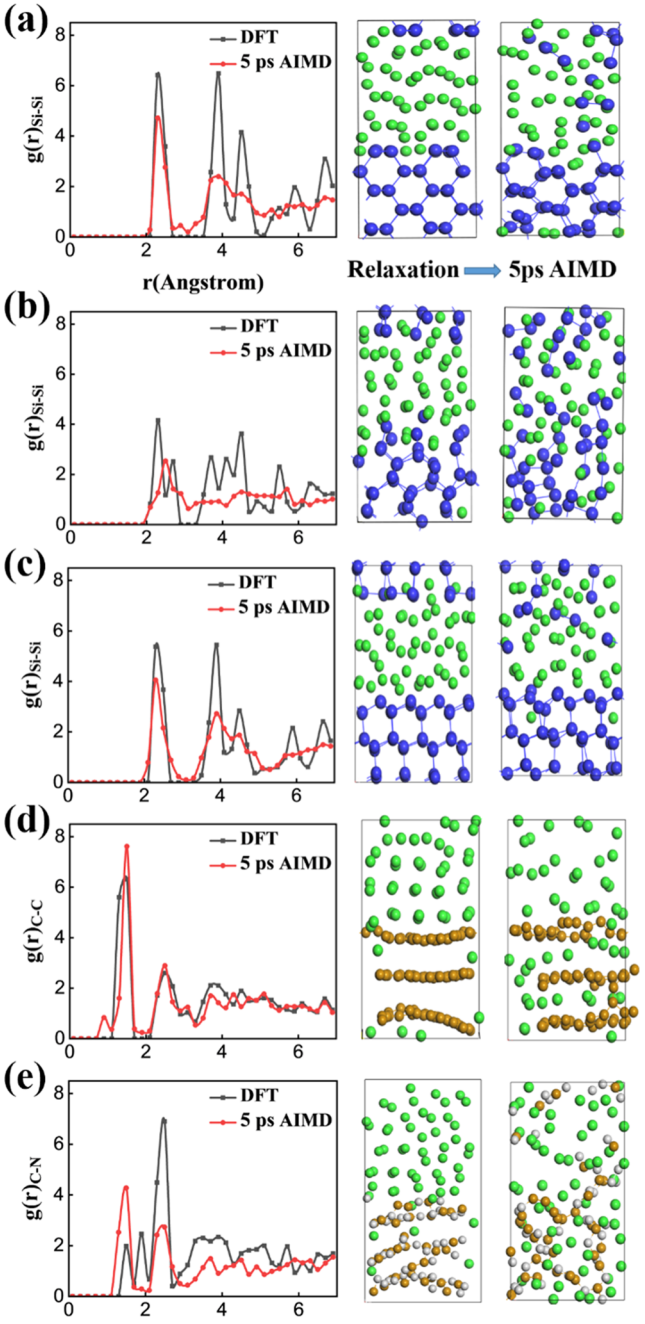

Figure 2. Atomic positions and RDF ($g(r)$) of the relaxed structure (initial state) and that after 5 ps of lithiation at 1200 K for (a) Si (100), (b) Si (110), (c) Si (111), (d) a-C, and (e) g-C_3N_4. The RDFs shown in (a)−(c) are for Si/Si pairs, (d) C/C pairs, and (e) C/N. The corresponding structural changes during the lithiation are specified for each case. Gray, blue, brown, and green spheres represent N, Si, and C atoms, and Li^+, respectively. All calculations were performed at 1200 K.

Thus, in Si (111), the diffusion of Li^+ is more difficult than that on other surfaces.

In the Si/C_3N_4 composite (Figure 4), C−N bonds were broken and the Li−C_3N_4 phase was formed during the lithiation process, which resulted in the complete disintegration of g-C_3N_4 in the initial stage (2.5−5 ps). It should be noted that Li^+ forces Li, C, and N atoms of the C−N phase to move toward the silicon anode, which, in turn, facilitates the replacement of the N holes in the anode. The electrochemical

https://doi.org/10.1021/acsomega.3c05523
ACS Omega 2023, 8, 44698−44707

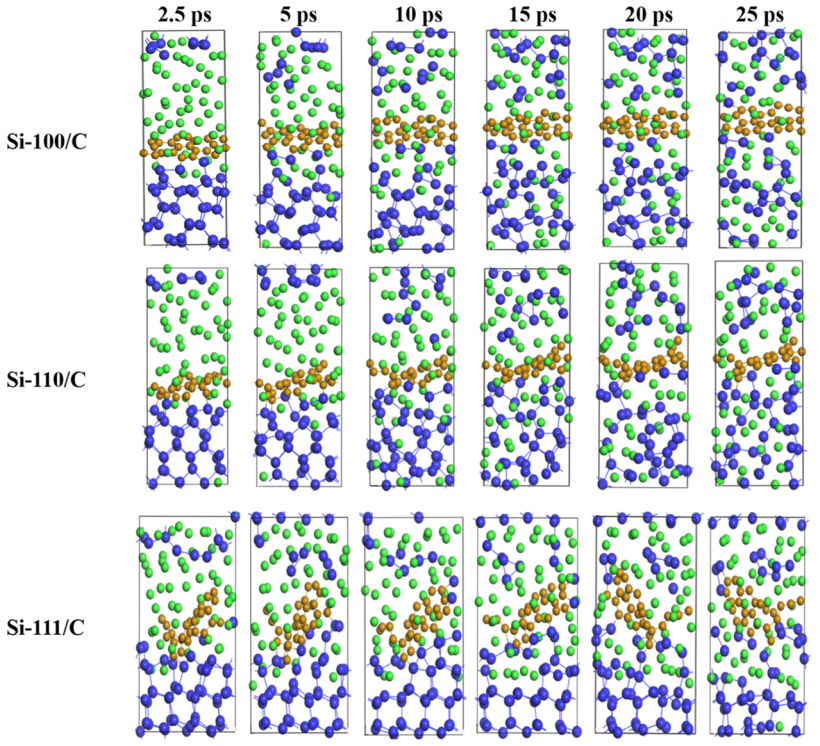

Figure 3. Structural snapshots of Li^+ diffusion in Si/C composites in three surfaces of Si at 1200 K at various simulation times during the lithiation process. Blue, brown, and green spheres represent Si, C, and Li^+, respectively.

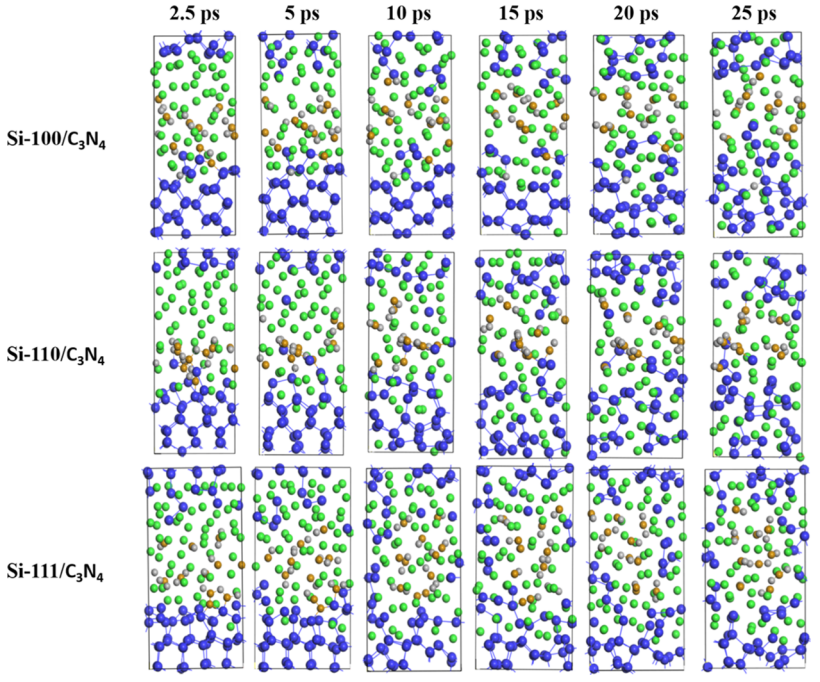

Figure 4. Structural snapshots of Li^+ diffusion in the Si/C_3N_4 composite (phases of $Li-C_3N_4$ for each Si surface) at 1200 K at some simulation times during the lithiation process. Gray, blue, brown, and green spheres represent N, Si, C, and Li^+, respectively.

insertion of Li^+ in interstitial crystalline Si prompts a crystalline-to-amorphous phase transition. Figure 4 shows the amorphous progression of crystalline boundaries as the Li content increases. The ratio of elements in the final phase is consistent with the very low dilute solubility of Li on Si surfaces. For the (100) and (110) surfaces, the amorphization involves the crystal breakdown into zigzag chains, with the chains being more ordered (aligned) for (110) than for (100). The zigzag chains appear as dumbbells for all surfaces and five-atom Si star nodes are observed for the (110) surface. In addition to ion transfer, components of the g-C_3N_4 phase also diffuse into Si lattice and act as single atom C binder and N hole. As shown in Figure 5, N-hole sites can be observed in the Li^+ diffusion pathway to the amorphous Si structure. Figures 3

https://doi.org/10.1021/acsomega.3c05523
ACS Omega 2023, 8, 44698−44707

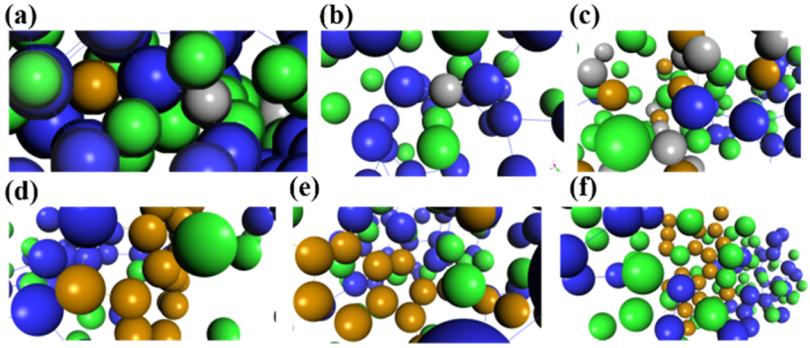

Figure 5. In situ of formation N hole and single-molecule C binder in the lithiation process of Si crystalline surface of (a) (100), (b) (110), and (c) (111) for Si/C_3N_4. The panels (d, f) are the same as (a, b), except for Si/C. In the case of Si/C, the C-layer acts as a barrier and results in the trapping of Li^+ for all three Si surfaces. Gray, blue, brown, and green spheres represent N, Si, C, and Li^+, respectively.

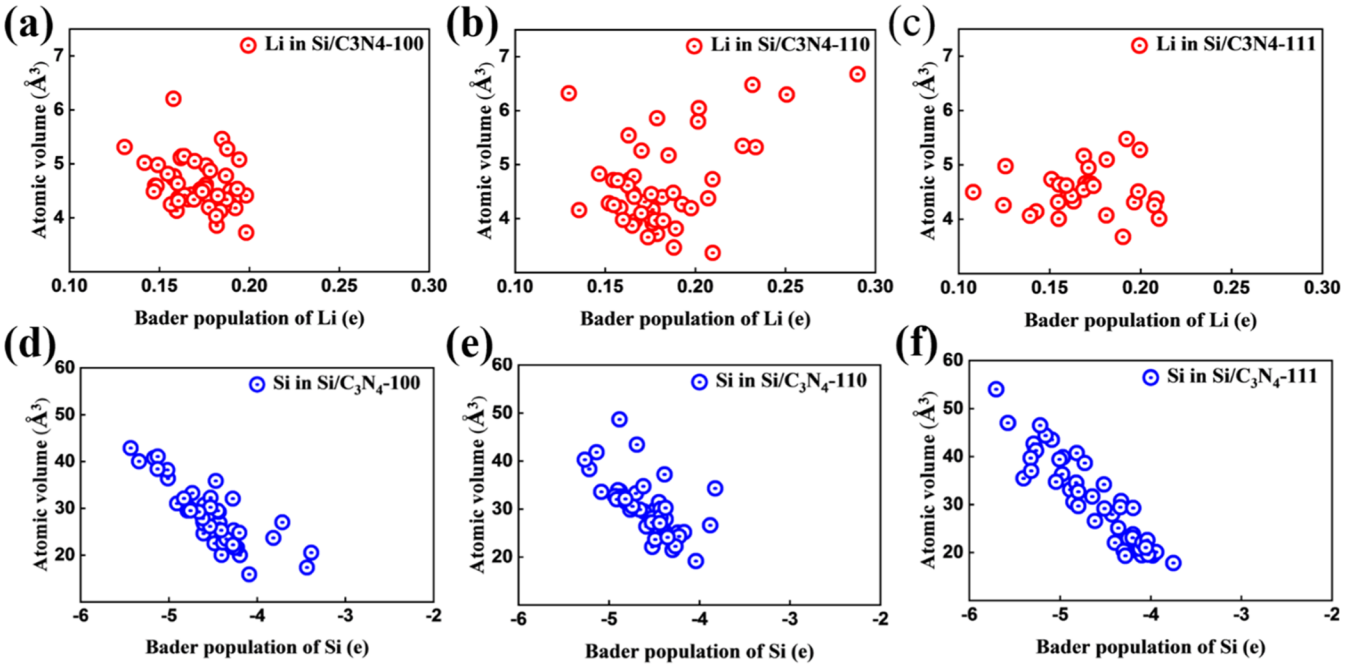

Figure 6. Atomic volume versus Bader populations of Li in (a) (100), (b) (110), and (c) (111) Si surface composites with C_3N_4. The panels (d, f) are the same as (a–c), except for atomic volume versus Bader populations of Si.

and 4 show the lithiation progress of the Si/C-layer and the Si/C_3N_4 composite, respectively. In the case of Si/C, the carbon layer does not suffer from significant distortion, whereas in the Si/C_3N_4 composite, the C_3N_4 layer disintegrates at the beginning of the lithiation. The guest lithium-ion diffusion is not the same along different orientations. During the lithiation in both studied compositions, different phases with three, four, and five Si nodes are formed.

Two ion-diffusion mechanisms, interstitial-mediated and vacancy-mediated, can be observed in Figure 5a–c.[15] Investigations of McBrayer et al.[33] and Zhou et al.[34] have shown that structural changes can lead to Li^+ site disorder, which in turn reduces the potential energy barrier for mobile Li^+ in fast-ion conductors. In other words, the insertion of Li^+ to high-energy sites reduces the energy barrier and induces ion migration in Li-rich phases.[33,34]

3.3. Quantitative Description of Lithiation Samples. For a more quantitative description of the lithiation process, Bader charge analyses were carried out. Figures 6 and 7 show atomic volume and partial charge distributions in various Si surfaces and composites that are caused by lithiation. It should be noted that a concentrated distribution indicates a more uniform Li-ion distribution. The obtained results show that ion permeation pathways induce fundamental changes to the structure of the Si electrode after the first lithiation. The formation of different phases in Si/Li/C and Si/Li/C_3N_4 anodes was investigated by using a radial distribution function (RDF). Li^+-diffusion coefficients were quantified by utilizing mean square displacement (MSD) calculations.

3.3.1. Bader Charge and Atomic Volume Analyses. Bader charge analysis provides the electron density contributions of various atoms,[35,36] which can be used to evaluate the volume changes and their distributions.[37−39] Figures 6 and 7 reveal that the atomic volume increase for Si (111) was the largest among other surfaces, whereas the lowest volume expansion was observed in Si (100). Bader charge plots demonstrate that after lithiation a wider variation was observed for Si (111), which was caused by the uneven distribution of Li^+ in the Si, while the Li^+ distribution is most concentrated in Si (100).

https://doi.org/10.1021/acsomega.3c05523
ACS Omega 2023, 8, 44698−44707

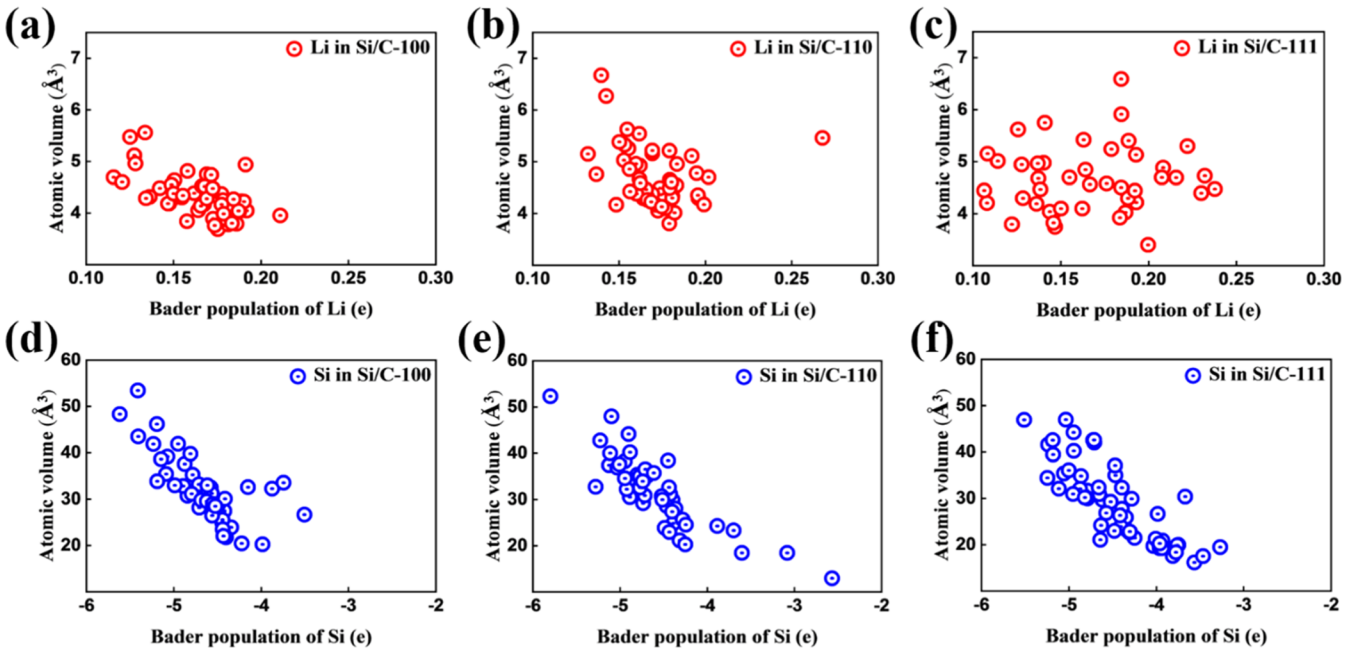

Figure 7. Atomic volume versus Bader populations of Li in (a) (100), (b) (110), and (c) (111) Si surface composites with the C-layer. The panels (d, f) are the same as (a–c), except for atomic volume versus Bader populations of Si.

Table 1. Bader Charge Analysis Results on Si (100), (110), and (111) Surfaces and Interfaces with Two Composites (C-Layer and C_3N_4)

interface model	*N* (Si)	*N* (Li)	*N* (C)	*N* (N)	average charge Si (e)	average charge Li (e)	average charge C (e)	average charge N (e)	average atomic volume Si (Å)
C_3N_4-100	48	48	15	9	4.49747	0.163645	3.536109	6.602125	28.11758
C_3N_4-110	48	48	15	9	4.50648	0.18583	3.367581	6.497625	29. 55175
C_3N_4-111	56	56	16	10	4.55746	0.183538	3.440599	6.418601	29.60694
C-100	48	48	24		4.65461	0.171496	4.360517		31.96457
C-110	48	48	24		4.62314	0.171258	4.455354		32.35513
C-111	56	56	26		4.45978	0.193392	4.537921		33.29199

The Si (111) surface is denser than other surfaces and the number of composite atoms in the interface is larger; therefore, the charge and atomic volume evaluation criteria were averaged for all samples for a fair comparison. Si/C_3N_4 composites present a smaller atomic volume in all three Si surfaces and offer a significant difference in partial charge for C atoms, see Table 1. In addition to Si surface orientation, N-holes and monatomic C binders enhanced the diffusion rate in the composite of Si/C_3N_4 during the lithiation process.

The average atomic volumes of Si listed in Table 1, which result in the total volume expansion,[47] depend on the charge state of the Si and Li^+. Figures 6 and 7 show that the atomic volume changes depend on the density of Si along the respective orientation. The total volume of samples can be obtained from the sum of the individual volume changes of Li^+ and Si. As a result, the total volume expansions of Si/C and Si/C_3N_4 composites originate from the distribution of charge states of Li^+ and Si as well as the Li^+ content in each Si crystalline orientation.

3.3.2. Pair Formation During Lithiation. Various amorphization stages for different crystalline orientations, as well as the evolution of the Li–Si and Li–Li correlations, are analyzed in this section. To distinguish the phases formed after lithiation and to further analyze the structural change during the lithiation process, RDF calculations for each compound were performed. The RDF is defined as the number of neighbor species as a function of distance per unit volume, which can provide important information regarding the diffusion and bond characteristics for both amorphous and crystalline solids.[26] For the composite with the C-layer, the RDF plots of Si/Si pairs of the initial structures (Figure 8a) exhibited different values for the studied Si surfaces, while the peaks almost overlapped because they depend on the material elements rather than the crystal orientation. After the completion of the lithiation process, the RDF plots show a transformation from the crystalline to the amorphous phase (Figure 8b).

Before lithiation, the first and the second nearest neighbors for Si/Si pairs in Si (100)/C_3N_4 peak at approximately 2.3 and 3.9 Å, respectively. It should be noted that the number of Si/Si pairs in these two cases is nearly equal (15 Si atoms) for the studied Si-surface orientation. After lithiation (Figure 8b), both the location of the peaks and the number of Si–Si pairs were slightly changed. Li/Si/C_3N_4 for Si (100) and (111) surfaces have a higher number of first nearest neighbors' Si/Si pairs than other samples. Moreover, a smoother peak for the second nearest neighbors in the Si (100)/C sample was observed, which can result in a nonhomogeneous ion diffusion.[40] The peaks of Si/Si pairs for the first and second nearest neighbors of the (110) surface in both composites were almost close to each other, indicating similar diffusivity in these two cases.

https://doi.org/10.1021/acsomega.3c05523
ACS Omega 2023, 8, 44698–44707

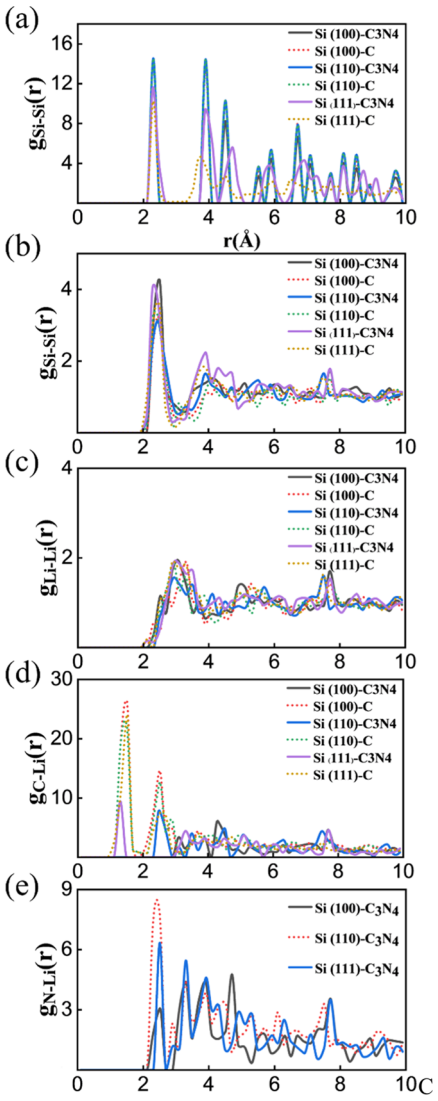

Figure 8. RDF of Si/C and Si/C/N composites for various Si crystalline surface orientations at 1200 K for (a) Si/Si pairs in the initial state, (b) Si/Si, (c) Li^+/Li^+, (d) C/Li^+, and (e) N/Li^+ pairs after lithiation.

The variations in the Li/Li pairs for different composites and Si-surface orientations provide useful insights into the diffusion process. Figure 8c shows that the pairs of Li/Li in the studied samples have different peak values as well as different peak locations. For the (110) surface in the Si/C_3N_4 composite, these differences are more pronounced than those on other surfaces. In this case, the second peak is smoother and shows a stronger Li diffusion for the (110) surface. For all Si surfaces with a C-layer, the existence of many Li/Li pairs can be attributed to the trapping and accumulation of Li^+. As shown in Figure 8d, the structure of the C-layer and the void at the Si/C interface cause the accumulation of Li^+ and more storage space than that of the C_3N_4 composite, which leads to a relatively large number of C/Li pairs.

The expansion of C-layers during lithiation can provide ideal spaces for Li^+ storage. As a result, the Si (100)/C exhibits the largest C/Li peaks as it possesses both the interfacial void and layered space, while Si (110)/C and Si (111)/C have similar C/Li peaks. On the other hand, the peaks of the Si/Li pairs show an opposite trend compared to C/Li pairs because a larger number of stored Li^+ in the C-layer leads to fewer Li^+ diffusing into the Si lattice. The RDF plots (Figure 8d) reveal that the interface atomic structure variation during the lithiation is more pronounced in the C_3N_4 composites than in the C-layer. In the case of the C-layer in comparison with the C_3N_4 composite, the structural uniformity was maintained during the lithiation process and acted as a barrier that resulted in the accumulation of Li^+.

In the Si/C-layer, all Li^+ must pass through the C-layer to diffuse into Si, affecting the atomic structure of the C-layer and the Si/C interface during the lithiation process, while in the C_3N_4 composite, a fraction of the Li^+ can directly diffuse into Si, partially reducing the primary barrier and energy for penetration into the Si structure. As shown in Figure 8e, N/Li pairs for various Si surfaces have different distributions of N vacancy and C monatomic binder, where the (110) surface shows a higher number of impurity pairs. Moreover, Li pairs with N were more frequent than those with host Si atoms. Therefore, the substitution of N with Si atoms can significantly improve guest ions trapped and nonmonovalent−isomorph intercalation.[41] Volume expansion during the Si lithiation is similar to the melting process, which transforms a solid to a liquid containing transient covalent bonds between neighboring atoms where a unique amorphous phase is formed.[42,43]

3.3.3. Li^+ Diffusivity. The MSD measures the deviation of the particle position with respect to a reference point over time and determines whether the ion is freely diffused or bonded.[38] To quantitatively define the diffusivity of Li in the Si/C-layer and Si/C_3N_4 composites, the MSDs of Li^+ were calculated by using

$$\mathrm{MSD} = \langle |r_i(t) - r_i(0)|^2 \rangle = \frac{1}{N}\sum_{i=1}^{N} |r_i(t) - r_i(0)|^2 \quad (1)$$

where $r_i(t)$ represents the positions of the specific atom at some time t, N is the total number of atoms, and the $\langle\rangle$ denotes the average over all of the atoms, see Figure 9. The diffusivity at a specific temperature is obtained from the MSD based on the Einstein relation

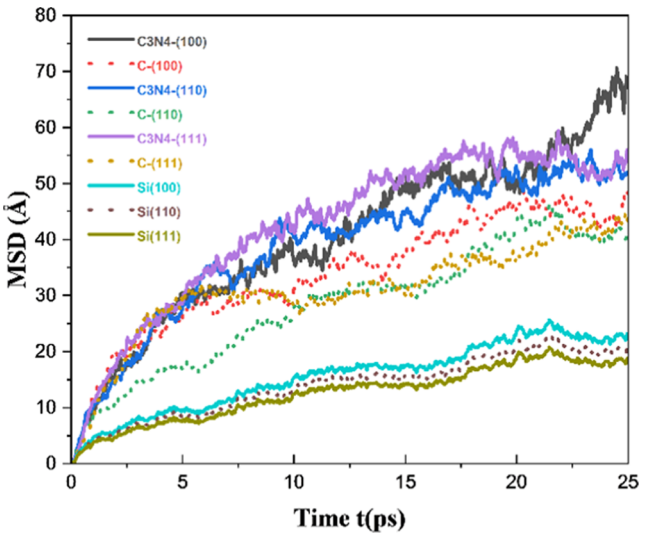

Figure 9. MSDs for Li^+ in the Si/C-layer, Si/C_3N_4 composites, and various Si surface orientations at 1200 K. The diffusivity is obtained by linear fits to the MSD curves. The fitting was performed for a time range between 15 and 22 ps to avoid initial transients.

https://doi.org/10.1021/acsomega.3c05523
ACS Omega 2023, 8, 44698−44707

$$D = \lim_{t\to\infty} \frac{\mathrm{MSD}}{nt} \quad (2)$$

where t is the total diffusion time and d is the number of dimensions.[27] The obtained diffusivities by linear fits to the MSD curves (Figure 9) are reported in Table 2.

Table 2. Calculated Diffusion Coefficients (cm^2/s) at 1200 K for Different Surfaces

type (surface)	pristine Si	Si/C composite	Si/C_3N_4 composite
Si (100)	7.82×10^{-5}	1.57×10^{-4}	3.17×10^{-4}
Si (110)	7.63×10^{-5}	1.32×10^{-4}	2.78×10^{-4}
Si (111)	7.45×10^{-5}	1.36×10^{-4}	2.69×10^{-4}

The diffusivity of bulk c-Si is approximately 7.82×10^{-5} cm^2/s at 1200 K, which is very close to the values reported by Gao et al.[4] For a more accurate understanding of the Li^+ conductivity rate in the examined samples, the MSD is reported in Table 2. The results show a significant difference between the Li^+-diffusion rates of various samples. Based on Table 2, the results indicate that the addition of the C-layer and C_3N_4 composites as amorphous layers improves the Li^+ diffusion in Si crystalline electrodes by a factor of 2 and ~4 for the C-layer and C_3N_4 composites, respectively. The Li^+ diffusivity enhancement in the Si/C composite depends on the orientation of the Si lattice. Li^+ diffusivity improvement for Si (100) is more than 16% larger than that of Si (111). Si surfaces with C_3N_4 composites contain large concentrations of surface C−N−C species that increase the Li^+ diffusivity. A nearly 400% increase in the Li^+ diffusion rate observed for Si/C_3N_4 compared to pristine Si highlights the impact of added species. The ion diffusivity enhancement in turn prevents void formation and volume expansion during lithiation. Figure 10a shows the Si (110)/C_3N_4 composite after complete lithiation, where Si with N hole replacement occurred, and Figure 10b depicts the same after the amorphization process, where the structural regularity shown in Figure 10a disappears.

g-C_3N_4 with a van der Waals layered structure has many structural defects and surface terminations that are added to each Si surface after lithiation disintegrates the Si lattice. N holes and monatomic C binder act as active sites for the enhancement of ion diffusion and create traps that improve electron conductivity.[44] In other cases in which only a single layer of carbon was added, electrons can pass through limited physical interfaces between conductive agents (e.g., conductive carbon) and other electrode components as a secondary conductive network.[45] Therefore, Si can tolerate large volume expansion with modified surface and Li^+ pathway by ion-diffusion improvement.[45]

4. CONCLUSIONS

In summary, the structural and interface changes for two C-layer and C_3N_4 composites as well as different Si host surface orientations were investigated from qualitative and quantitative approaches during lithiation by employing DFT and AIMD calculations. The effects of ion distribution on volume expansion and partial charge were analyzed. In the Si/C-layer composite, Li^+ was forced to pass through the C-layer first; thus, the diffusion rate is strongly dependent on the C-layer and Si surface characteristics. The Si/C_3N_4 composite exhibits a larger Li^+ diffusivity than the C-layer. Bader calculations provide useful insights into atomic volumes, partial charges, and Li^+ distribution. The RDF results for all composites further explained the structural evolution during the lithiation process and confirmed that the initial structure of the C-layer and Si/C_3N_4 composites affect the Li^+-diffusion process. It was revealed that the Li^+ diffusion in the Si material was enhanced by the addition of a C_3N_4 composite in three Si surfaces, while the enhancement was stronger in the Si (100) composite. For C_3N_4 composites, the atomic structures significantly affected Li^+ diffusion. These results provide key insights into the fundamental mechanism of Li^+ diffusion in Si/C and Si/C/N ternary composite materials and pave the way for realizing safe and fast-charging lithium-ion batteries.

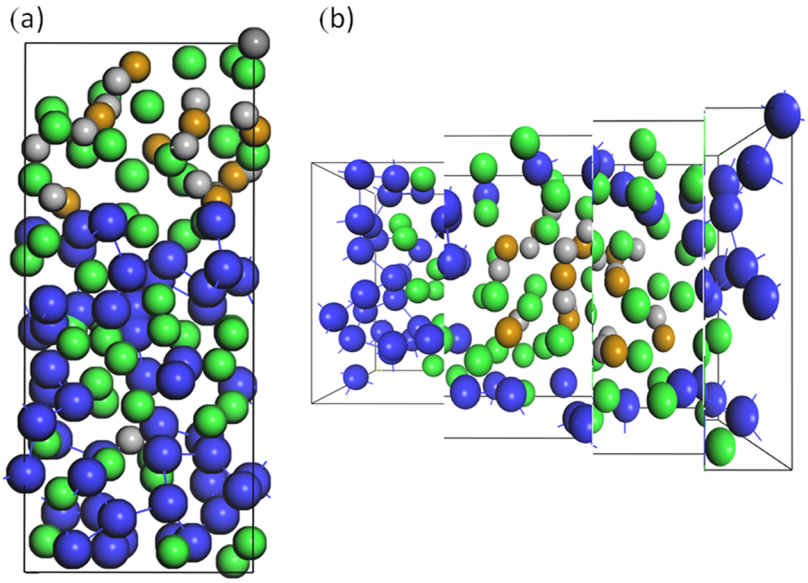

Figure 10. (a) Atomic configurations after the lithiation of the Si (110)/C_3N_4 composite and (b) after the amorphization process. Gray, blue, brown, and green spheres N, Si, C, and Li^+, respectively. For better observation of molecules, the studied cell in (b) was horizontally regenerated.

https://doi.org/10.1021/acsomega.3c05523
ACS Omega 2023, 8, 44698−44707

AUTHOR INFORMATION

Corresponding Authors

Zeinab Sanaee − *School of Electrical and Computer Engineering, College of Engineering, University of Tehran, Tehran 14395-515, Iran;* orcid.org/0000-0002-1966-032X; Email: z.sanaee@ut.ac.ir

Mahdi Pourfath − *School of Electrical and Computer Engineering, College of Engineering, University of Tehran, Tehran 14395-515, Iran; Institute for Microelectronics/E360, TU Wien, A-1040 Vienna, Austria;* orcid.org/0000-0002-8053-578X; Email: pourfath@ut.ac.ir

Authors

Ali Lashani Zand − *School of Electrical and Computer Engineering, College of Engineering, University of Tehran, Tehran 14395-515, Iran;* orcid.org/0000-0003-1711-5704

Amin Niksirat − *School of Electrical and Computer Engineering, College of Engineering, University of Tehran, Tehran 14395-515, Iran;* orcid.org/0009-0006-8083-4698

Complete contact information is available at: https://pubs.acs.org/10.1021/acsomega.3c05523

Notes

The authors declare no competing financial interest.

ACKNOWLEDGMENTS

The authors would like to express their gratitude for the computing resources generously made available by the Super Computing Institute at the University of Tehran.

REFERENCES

(1) Chen, H.; Zhou, G.; Boyle, D.; Wan, J.; Wang, H.; Lin, D.; Mackanic, D.; Zhang, Z.; Kim, S. C.; Lee, H. R.; Wang, H.; Huang, W.; Ye, Y.; Cui, Y. Electrode Design with Integration of High Tortuosity and Sulfur-Philicity for High-Performance Lithium-Sulfur Battery. *Matter* **2020**, *2* (6), 1605−1620.

(2) Cheetham, A. K.; Seshadri, R.; Wudl, F. Chemical synthesis and materials discovery. *Nat. Synth.* **2022**, *1*, 514−520.

(3) Gao, X.; Lu, W.; Xu, J. Insights into the Li diffusion mechanism in Si/C composite anodes for lithium-ion batteries. *ACS Appl. Mater. Interfaces* **2021**, *13*, 21362−21370.

(4) Huo, H.; Janek, J. Silicon as Emerging Anode in Solid-State Batteries. *ACS Energy Lett.* **2022**, *7*, 4005−4016.

(5) Cui, Y. Silicon anodes. *Nat. Energy* **2021**, *6*, 995−996.

(6) Wang, C.-Y.; Liu, T.; Yang, X.-G.; Ge, S.; Stanley, N. V.; Rountree, E. S.; Leng, Y.; McCarthy, B. D. Fast charging of energy-dense lithium-ion batteries. *Nature* **2022**, *611*, 485−490.

(7) Wang, C.; Wu, H.; Chen, Z.; McDowell, M. T.; Cui, Y.; Bao, Z. Self-healing chemistry enables the stable operation of silicon microparticle anodes for high-energy lithium-ion batteries. *Nature Chem.* **2013**, *5*, 1042−1048.

(8) Juzeliunas, E.; Fray, D. J. Silicon electrochemistry in molten salts. *Chem. Rev.* **2020**, *120*, 1690−1709.

(9) Tan, D. H.; Chen, Y. T.; Yang, H.; et al. Carbon-free high-loading silicon anodes enabled by sulfide solid electrolytes. *Science* **2021**, *373*, 1494−1499, DOI: 10.1126/science.abg7217.

(10) Wang, H.; Ji, X.; Chen, C.; Xu, K.; Miao, L. Lithium diffusion in silicon and induced structure disorder: A molecular dynamics study. *AIP Adv.* **2013**, *3*, No. 112102.

(11) Basu, S.; Suresh, S.; Ghatak, K.; Bartolucci, S. F.; Gupta, T.; Hundekar, P.; Kumar, R.; Lu, T.-M.; Datta, D.; Shi, Y.; Koratkar, N. Utilizing van der Waals slippery interfaces to enhance the electrochemical stability of silicon film anodes in lithium-ion batteries. *ACS Appl. Mater. Interfaces* **2018**, *10* (16), 13442−13451, DOI: 10.1021/acsami.8b00258.

(12) Stournara, M. E.; Qi, Y.; Shenoy, V. B. From ab initio calculations to multiscale design of Si/C core−shell particles for Li-ion anodes. *Nano Lett.* **2014**, *14*, 2140−2149.

(13) Johari, P.; Qi, Y.; Shenoy, V. B. The mixing mechanism during lithiation of Si negative electrode in Li-ion batteries: an ab initio molecular dynamics study. *Nano Lett.* **2011**, *11*, 5494−5500.

(14) Stournara, M. E.; Xiao, X.; Qi, Y.; Johari, P.; Lu, P.; Sheldon, B. W.; Gao, H.; Shenoy, V. B. Li segregation induces structure and strength changes at the amorphous Si/Cu interface. *Nano Lett.* **2013**, *13*, 4759−4768.

(15) Qu, J.; Ning, C.; Feng, X.; Yao, B.; Liu, B.; Lu, Z.; Wang, T.; Seh, Z. W.; Shi, S.; Zhang, Q. Identifying Hidden Li−Si−O Phases for Lithium-Ion Batteries via First-Principle Thermodynamic Calculations. *Energy Environ. Mater.* **2022**, *5*, 865−871.

(16) Khossossi, N.; Singh, D.; Banerjee, A.; Luo, W.; Essaoudi, I.; Ainane, A.; Ahuja, R. Highspecific-capacity and high-performing post-lithium-ion battery anode over 2D black arsenic phosphorus. *ACS Appl. Energy Mater.* **2021**, *4*, 7900−7910.

(17) Veith, G. M.; Baggetto, L.; Adamczyk, L. A.; Guo, B.; Brown, S. S.; Sun, X.-G.; Albert, A. A.; Humble, J. R.; Barnes, C. E.; Bojdys, M. J.; Dai, S.; Dudney, N. J. Electrochemical and solid-state lithiation of graphitic C3N4. *Chem. Mater.* **2013**, *25* (3), 503−508, DOI: 10.1021/cm303870x.

(18) Sung, J.; Kim, N.; Ma, J.; et al. Subnano-sized silicon anode via crystal growth inhibition mechanism and its application in a prototype battery pack. *Nat. Energy* **2021**, *6*, 1164−1175.

(19) Shih, J.-Y.; Chen, Y.-R.; James Li, Y.-J.; Hung, T.-F.; Hsu, L.-F.; Tsai, Y.-D.; Ramaraj, S. K.; Jose, R.; Karuppiah, C.; Yang, C.-C. Suppressed Volume Change of a Spray-Dried 3D Spherical-like Si/Graphite Composite Anode for High-Rate and Long-Term Lithium-Ion Batteries. *ACS Sustainable Chem. Eng.* **2022**, *10*, 12706−12720.

(20) Shi, X.; Zhu, J.; Xia, Y.; Fan, F.; Zhang, F.; Gu, M.; Yang, H. Ultrahigh malleability of the lithiation-induced Li x Si phase. *ACS Appl. Energy Mater.* **2018**, *1*, 4211−4220.

(21) Seidlhofer, B.-K.; Jerliu, B.; Trapp, M.; Huger, E.; Risse, S.; Cubitt, R.; Schmidt, H.; Steitz, R.; Ballauff, M. Lithiation of crystalline silicon as analyzed by operando neutron reflectivity. *ACS Nano* **2016**, *10*, 7458−7466.

(22) Li, J.; Dahn, J. An in situ X-ray diffraction study of the reaction of Li with crystalline Si. *J. Electrochem. Soc.* **2007**, *154*, A156.

(23) Cao, C.; Shyam, B.; Wang, J.; Toney, M. F.; Steinruck, H.-G. Shedding X-ray light on the interfacial electrochemistry of silicon anodes for Li-ion batteries. *Acc. Chem. Res.* **2019**, *52*, 2673−2683.

(24) Key, B.; Morcrette, M.; Tarascon, J.-M.; Grey, C. P. Pair distribution function analysis and solid state NMR studies of silicon electrodes for lithium ion batteries: understanding the (de) lithiation mechanisms. *J. Am. Chem. Soc.* **2011**, *133*, 503−512.

(25) Sun, J.; Remsing, R.; Zhang, Y.; et al. Accurate first-principles structures and energies of diversely bonded systems from an efficient density functional. *Nat. Chem.* **2016**, *8*, 831−836.

(26) Chan, M. K. Y.; Wolverton, C.; Greeley, J. P. First principles simulations of the electrochemical lithiation and delithiation of faceted crystalline silicon. *J. Am. Chem. Soc.* **2012**, *134*, 14362−14374.

(27) Jain, R.; Lakhnot, A. S.; Bhimani, K.; Sharma, S.; Mahajani, V.; Panchal, R. A.; Kamble, M.; Han, F.; Wang, C.; Koratkar, N. Nanostructuring versus microstructuring in battery electrodes. *Nat. Rev. Mater.* **2022**, *7*, 736−746.

(28) Luo, H.; Yu, P.; Li, G.; Yan, K. Topological quantum materials for energy conversion and storage. *Nat. Rev. Phys.* **2022**, *4*, 611−624.

(29) Gao, Y.; Rojas, T.; Wang, K.; Liu, S.; Wang, D.; Chen, T.; Wang, H.; Ngo, A. T.; Wang, D. Low-temperature and high-rate-charging lithium metal batteries enabled by an electrochemically active monolayer-regulated interface. *Nat. Energy* **2020**, *5*, 534−542.

(30) Kaltak, M.; Klimeš, J.; Kresse, G. Cubic scaling algorithm for the random phase approximation: Self-interstitials and vacancies in Si. *Phys. Rev. B* **2014**, *90*, No. 054115.

(31) Batchelder, D. N.; Simmons, R. Lattice constants and thermal expansivities of silicon and of calcium fluoride between 6 and 322 K. *J. Chem. Phys.* **1964**, *41*, 2324−2329.
(32) Zhou, L.; Assoud, A.; Zhang, Q.; Wu, X.; Nazar, L. F. New family of argyrodite thioantimonate lithium superionic conductors. *J. Am. Chem. Soc.* **2019**, *141*, 19002−19013.
(33) Zhou, L.; Minafra, N.; Zeier, W. G.; Nazar, L. F. Innovative approaches to Li-argyrodite solid electrolytes for all-solid-state lithium batteries. *Acc. Chem. Res.* **2021**, *54*, 2717−2728.
(34) McBrayer, J. D.; Rodrigues, M. T. F.; Schulze, M. C.; et al. Calendar aging of silicon-containing batteries. *Nat. Energy* **2021**, *6*, 866−872.
(35) Tang, W.; Sanville, E.; Henkelman, G. A grid-based Bader analysis algorithm without lattice bias. *J. Phys.: Condens. Matter* **2009**, *21*, No. 084204.
(36) Sanville, E.; Kenny, S. D.; Smith, R.; Henkelman, G. Improved grid-based algorithm for Bader charge allocation. *J. Comput. Chem.* **2007**, *28*, 899−908.
(37) Henkelman, G.; Arnaldsson, A.; Jónsson, H. A fast and robust algorithm for Bader decomposition of charge density. *Comput. Mater. Sci.* **2006**, *36*, 354−360.
(38) Yu, M.; Trinkle, D. R. Accurate and efficient algorithm for Bader charge integration. *J. Chem. Phys.* **2011**, *134*, No. 064111, DOI: 10.1063/1.3553716.
(39) Gatti, C.; Fantucci, P. Are Bader electron populations atomic size dependent? *J. Phys. Chem. A* **1993**, *97*, 11677−11680.
(40) Ye, X.; Gan, C.; Huang, L.; Qiu, Y.; Xu, Y.; Huang, L.; Luo, X. Improving Lithium-Ion Diffusion Kinetics in Nano-Si@ C Anode Materials with Hierarchical MoS2 Decoration for High-Performance Lithium-Ion Batteries. *ChemElectroChem* **2021**, *8*, 1270−1279.
(41) Zhu, Bin.; Liu, G.; Lv, G.; et al. Minimized lithium trapping by isovalent isomorphism for high initial Coulombic efficiency of silicon anodes. *Sci. Adv.* **2019**, *5*, No. eaax0651.
(42) Hou, G.; Cheng, B.; Yang, Y.; Du, Y.; Zhang, Y.; Li, B.; He, J.; Zhou, Y.; Yi, D.; Zhao, N.; Bando, Y.; Golberg, D.; Yao, J.; Wang, X.; Yuan, F. Multiscale buffering engineering in silicon−carbon anode for ultrastable Li-ion storage. *ACS Nano* **2019**, *13* (9), 10179−10190, DOI: 10.1021/acsnano.9b03355.
(43) Wuttig, M. Revisiting the nature of chemical bonding in chalcogenides to explain and design their properties. *Adv. Mater.* **2022**, No. 2208485.
(44) Chen, S.; Song, Z.; Wang, L.; Chen, H.; Zhang, S.; Pan, F.; Yang, L. Establishing a resilient conductive binding network for Si-based anodes via molecular engineering. *Acc. Chem. Res.* **2022**, *55*, 2088−2102.
(45) Pan, S.; Han, J.; Wang, Y.; Li, Z.; Chen, F.; Guo, Y.; Han, Z.; Xiao, K.; Yu, Z.; Yu, M.; Wu, S.; Wang, D.-W.; Yang, Q.-H. Integrating SEI into layered conductive polymer coatings for ultrastable silicon anodes. *Adv. Mater.* **2022**, *34*, No. 2203617, DOI: 10.1002/adma.202203617.
(46) Perdew, J. P.; Burke, K.; Ernzerhof, M. Generalized gradient approximation made simple. *Phys. Rev. Lett.* **1996**, *77* (18), 3865 DOI: 10.1103/PhysRevLett.77.3865.
(47) Bäker, M. understanding element solution energies in nickelbase alloys using machine learning. *Mater. Res. Express* **2023**, *10*, No. 036503.

https://doi.org/10.1021/acsomega.3c05523
ACS Omega 2023, 8, 44698−44707